ISSN 1674-1056
http://cpb.iphy.ac.cn
http://iopscience.iop.org/cpb
中国物理 B
Chinese Physics
中国物理 Chinese Physics B

Pulling force of acoustic-vortex beams on centered elastic spheres based on the annular transducer model

Yuzhi Li(李禹志), Qingdong Wang(王青东), Gepu Guo(郭各朴), Hongyan Chu(褚红燕), Qingyu Ma(马青玉), Juan Tu(屠娟), Dong Zhang(章东)
Citation: Chin. Phys. B . 2020, 29(5): 054302 . **doi:** 10.1088/1674-1056/ab8210
Journal homepage: http://cpb.iphy.ac.cn; http://iopscience.iop.org/cpb

What follows is a list of articles you may be interested in

Axial acoustic radiation force on a fluid sphere between two impedance boundaries for Gaussian beam

Yuchen Zang(臧雨宸), Yupei Qiao(乔玉配), Jiehui Liu(刘杰惠), Xiaozhou Liu(刘晓宙)
Chin. Phys. B . 2019, 28(3): 034301 . **doi:** 10.1088/1674-1056/28/3/034301

Acoustic radiation force on a multilayered sphere in a Gaussian standing field

Haibin Wang(汪海宾), Xiaozhou Liu(刘晓宙), Sha Gao(高莎), Jun Cui(崔骏), Jiehui Liu(刘杰惠), Aijun He(何爱军), Gutian Zhang(张古田)
Chin. Phys. B . 2018, 27(3): 034302 . **doi:** 10.1088/1674-1056/27/3/034302

Acoustic radiation force induced by two Airy-Gaussian beams on a cylindrical particle

Sha Gao(高莎), Yiwei Mao(毛一葳), Jiehui Liu(刘杰惠), Xiaozhou Liu(刘晓宙)
Chin. Phys. B . 2018, 27(1): 014302 . **doi:** 10.1088/1674-1056/27/1/014302

Acoustic scattering from a submerged cylindrical shell coated with locally resonant acoustic metamaterials

Li Li, Wen Ji-Hong, Cai Li, Zhao Hong-Gang, Wen Xi-Sen
Chin. Phys. B . 2013, 22(1): 014301 . **doi:** 10.1088/1674-1056/22/1/014301

Pulling force of acoustic-vortex beams on centered elastic spheres based on the annular transducer model*

Yuzhi Li(李禹志)[1], Qingdong Wang(王青东)[2], Gepu Guo(郭各朴)[1], Hongyan Chu(褚红燕)[1], Qingyu Ma(马青玉)[1,†], Juan Tu(屠娟)[3], and Dong Zhang(章东)[3]

[1] *School of Physics and Technology, Nanjing Normal University, Nanjing* 210023, *China*
[2] *College of Ocean Science and Engineering, Shandong University of Science and Technology, Qingdao* 266590, *China*
[3] *Institute of Acoustics, Nanjing University, Nanjing* 210093, *China*

(Received 3 February 2020; revised manuscript received 21 February 2020; accepted manuscript online 23 March 2020)

To solve the difficulty of generating an ideal Bessel beam, an simplified annular transducer model is proposed to study the axial acoustic radiation force (ARF) and the corresponding negative ARF (pulling force) exerted on centered elastic spheres for acoustic-vortex (AV) beams of arbitrary orders. Based on the theory of acoustic scattering, the axial distributions of the velocity potential and the ARF for AV beams of different orders generated by the annular transducers with different physical sizes are simulated. It is proved that the pulling force can be generated by AV beams of arbitrary orders with multiple axial regions. The pulling force is more likely to exert on the sphere with a smaller k_0a (product of the wave number and the radius) for the AV beam with a bigger topological charge due to the strengthened off-axis acoustic scattering. The pulling force decreases with the increase of the axial distance for the sphere with a bigger k_0a. More pulling force areas with wider axial regions can be formed by AV beams using a bigger-sized annular transducer. The theoretical results demonstrate the feasibility of generating the pulling force along the axes of AV beams using the experimentally applicable circular array of planar transducers, and suggest application potentials for multi-position stable object manipulations in biomedical engineering.

Keywords: acoustic radiation force, pulling force, acoustic-vortex beams, annular transducer model, acoustic scattering

PACS: 43.25.Qp, 43.60.Fg, 43.38.Hz **DOI:** 10.1088/1674-1056/ab8210

1. Introduction

As a special kind of acoustic field with helical wave front and center pressure null[1,2] along the propagation axis, acoustic-vortex (AV) beams have been proved to possess the capability of object manipulation due to the orbital angular momentum (OAM)[3–9] transfer. For the AV beam with a nonzero topological charge, objects can be trapped[10–13] non-destructively to the vortex center in a rotation manner, showing promising prospects in biophysical and biomedical applications. Although the manipulation performances of AV beams in the transverse plane have been demonstrated theoretically and experimentally, the axial property remains great significance for stable object manipulations in three dimensions. Related investigations on the axial acoustic radiation force (ARF) were conducted to analyze the positive (pushing) and negative (pulling) forces for acoustical tweezers. By utilizing the ray acoustics approach, the pulling force generated by a strongly focused 100-MHz ultrasonic transducer with a Gaussian intensity distribution[14] was theoretically studied, and the feasibility of acoustical tweezers was demonstrated to depend on both the acoustic impedance mismatch and the degree of focusing relative to the particle size. The radiation forces generated by plane waves, Bessel beams, and arbitrary beams on elastic spheres in a liquid or gas medium were formulated.[15] The axial distributions of the ARF and the negative ARF of a focused transducer in the form of a spherical cap and a multi-element linear array were discussed in detail. The ARF exerted on a spherical target by an ideal zero-order standing or quasi-standing Bessel beam[16] was reported. The pulling (attractive) force was proved to be diminished by the viscoelasticity of objects and the increasing of the half-cone angle β. The generation of the negative ARF was investigated using a limited-diffracting single annular piezo-ring transducer. Numerical computations were performed for various types of spheres. The acoustic beam generated by an annular-ring circular transducer[17] was proved to be capable of inducing a pulling force over an extended region in space. By employing the paraxial approximation, it was demonstrated that Rayleigh particles could be trapped in the pre-focal zone[18] along the beam axis with the pulling force of nano-newtons range. However, for the absence of the azimuthal phase factor,[19] the axial manipulation capability was only investigated for the Gaussian or Bessel beams of zero-order.

Further investigations on the ARF generated by specific AV beams were also conducted. By using the far-field limit, the exact scattering by spheres with different boundaries cen-

*Project supported by the National Natural Science Foundation of China (Grant Nos. 11934009, 11974187, and 11604156).
†Corresponding author. E-mail: maqingyu@njnu.edu.cn
© 2020 Chinese Physical Society and IOP Publishing Ltd

tered on a Bessel beam[20] were deduced. Based on the proposed terminology of the negative ARF island, additional examples of the zero-order Bessel beam[21] and the helicoidal Bessel beam[22] were presented. The pulling force islands for various β and k_0a (the product of the wave number and the radius of the sphere) were proved to be correlated with the conditions giving reduced backscattering by the sphere. The negative ARFs of Bessel beams and non-diffracting beams were geometrically interpreted,[23,24] clearing that the negative force conditions were directly related to the suppressed acoustic scattering in the backwards hemisphere. The pulling force of standing wave tweezers of a high-order Bessel beam on a rigid sphere[25–27] was reported to be weakened by the increase of β. In addition, micro-particles placed on a thin film were axially manipulated[28] by the focused AV beam of first-order using a spherical array of 127 transducers.

Although the pulling force was discussed in previous studies, the ideal Bessel AV beam could not be generated easily according to the conclusion[29] made by McGloin and Dholakia. As demonstrated by Marston, the Bessel approximation[20,21] was only proper when the distance between the sphere and the source was less than $a_T/\tan\beta$, and the incident wave was no longer a Bessel beam when close-to and beyond the distance, where a_T was the radius of the source. Therefore, the ideal Bessel beams of arbitrary orders are difficult to generate in experiment and the corresponding conclusion of the pulling force is meaningless in practical applications. More attentions should be focused on the pulling force of AV beams using an experimentally applicable transducer array.

In this paper, the pulling force exerted on elastic spheres centered on AV beams generated by an annular transducer model is investigated. By considering the acoustic scattering from spheres with various k_0a, axial distributions of the ARF and the corresponding pulling force for AV beams generated by the annular transducers with different physical sizes are simulated. It is proved that the pulling force can be generated along the axis of the AV beam of an arbitrary order with multiple axial regions, and it is more likely to exert on the sphere with a smaller k_0a for the AV beam of a higher-order. More pulling force areas with wider axial regions and higher force amplitudes can be formed by a bigger-sized annular transducer. The favorable results demonstrate the feasibility of generating the pulling force along the axes of AV beams, and suggest application potentials of stable object manipulations using an experimentally applicable circular array of planar sources.

2. Principle and method

The schematic diagram of the ARF analysis for AV beams generated by the annular transducer is illustrated in Fig. 1. In the spherical coordinates, an elastic sphere is placed at the origin O, and an annular transducer with the outer and inner radii of r_b and r_a is placed at $z=-z_0$, being perpendicular to the z axis. The radius and the width of the annular transducer are set to $r_\mathrm{base}=(r_\mathrm{b}+r_\mathrm{a})/2$ and $W=r_\mathrm{b}-r_\mathrm{a}$, respectively. To generate an AV beam along the center axis with the topological charge m, the phase term $\exp(\mathrm{i}m\varphi_\mathrm{s})$ is introduced to provide the circular phase variation along the azimuthal direction, where φ_s is the azimuthal angle of the surface element $P_\mathrm{s}(r_\mathrm{s},\theta_\mathrm{s},\varphi_\mathrm{s})$. For the acoustic wave radiated by $P_\mathrm{s}(r_\mathrm{s},\theta_\mathrm{s},\varphi_\mathrm{s})$, the incident velocity potential at the observation point $P(r,\theta,\varphi)$ can be described by

$$\phi_i(r,\theta,\varphi)=\frac{u_0\exp(k_0R-\omega t)}{R}\cdot\exp(\mathrm{i}m\varphi_\mathrm{s}), \tag{1}$$

where u_0 is the vibrating velocity[11] on the transducer surface, R is the distance from $P(r,\theta,\varphi)$ to $P_\mathrm{s}(r_\mathrm{s},\theta_\mathrm{s},\varphi_\mathrm{s})$, ω is the angular frequency, $k_0=\omega/c_0$ and c_0 are the wave number and the acoustic speed in water, respectively. Thus, the incident velocity potential produced by the transducer can be calculated by

$$\phi_i(r,\theta,\varphi)=\iint_S\frac{u_0\exp(k_0R-\omega t)}{R}\exp(\mathrm{i}m\varphi_\mathrm{s})\cdot\mathrm{d}S, \tag{2}$$

where $\mathrm{d}S=r_0\mathrm{d}r_0\mathrm{d}\varphi_\mathrm{s}$, r_0 and φ_s are the integral variables on the transducer surface. In the spherical coordinates, for $a<r<r_\mathrm{inner}$, the incident velocity potential can be rewritten as[30]

$$\begin{aligned}&\phi_i(r,\theta,\varphi)\\&=\mathrm{e}^{-\mathrm{i}\omega t}\sum_{n=0}^{\infty}\mathrm{i}\cdot u_0k_0\frac{(2n+1)}{4\pi}\int_0^{2\pi}\int_{r_\mathrm{a}}^{r_\mathrm{b}}\exp(\mathrm{i}m\varphi_\mathrm{s})\mathrm{P}_n(\cos\Gamma)\\&\times\mathrm{h}_n(k_0r_\mathrm{s})\mathrm{j}_n(k_0r)\cdot r_0\mathrm{d}r_0\mathrm{d}\varphi_\mathrm{s},\end{aligned} \tag{3}$$

where r_inner is the distance from an arbitrary point on the inner boundary of the annular transducer to the center O of the sphere, and Γ is the angle between OP and OP_s, $\mathrm{j}_n(x)$, $\mathrm{h}_n(x)$, and $\mathrm{P}_n(x)$ are the spherical Bessel function, the spherical Hankel function of the first kind, and the Legendre polynomial of the n-th order, respectively. Thus, the velocity potential scattered by the sphere in the defined area is achieved by

$$\begin{aligned}\phi_\mathrm{s}(r,\theta,\varphi)=\mathrm{e}^{-\mathrm{i}\omega t}\sum_{n=0}^{\infty}\mathrm{i}\cdot u_0k_0\frac{(2n+1)}{4\pi}s_n\mathrm{h}_n(k_0r)\cdot\mathrm{h}_n(k_0r_\mathrm{s})\\\times\int_0^{2\pi}\int_{r_\mathrm{a}}^{r_\mathrm{b}}\mathrm{P}_n(\cos\Gamma)\exp(\mathrm{i}m\varphi_\mathrm{s})\cdot r_0\mathrm{d}r_0\mathrm{d}\varphi_\mathrm{s},\end{aligned} \tag{4}$$

where

$$s_n=-\left[\frac{\mathrm{j}_n'(k_0a)+\mathrm{i}\beta\mathrm{j}_n(k_0a)}{\mathrm{h}_n'(k_0a)+\mathrm{i}\beta\mathrm{h}_n(k_0a)}\right],\quad\beta_l=\mathrm{i}\cdot\frac{\rho_0c_0}{\rho_\mathrm{s}c_\mathrm{s}}\cdot\frac{\mathrm{j}_l'(k_\mathrm{s}a)}{\mathrm{j}_l(k_\mathrm{s}a)}$$

is determined by the impedance difference between the sphere and the surrounding water.[31] ρ_s, c_s, and k_s are the density, the acoustic speed, and the wave number of the sphere, respectively. Based on the Legendre expression[32,33] $\mathrm{P}_n(\cos\Gamma)=$

$\frac{4\pi}{2n+1}\sum_{l=-n}^{n}\mathrm{Y}_{nl}(\theta,\varphi)\mathrm{Y}^{*}_{nl}(\theta_\mathrm{s},\varphi_\mathrm{s})$ and the definition of spherical harmonics, the integral term can be replaced by the associate Legendre function as

$$\begin{aligned}&\frac{4\pi}{2n+1}\int_0^{2\pi}\sum_{l=-n}^{n}\mathrm{Y}_{nl}(\theta,\varphi)\,\mathrm{Y}^{*}_{nl}(\theta_\mathrm{s},\varphi_\mathrm{s})\exp(\mathrm{i}m\varphi_\mathrm{s})\,\mathrm{d}\varphi_\mathrm{s}\\ =\;&\frac{4\pi}{2n+1}\sum_{l=-n}^{n}\int_0^{2\pi}\mathrm{Y}_{nl}(\theta,\varphi)\sqrt{\frac{2n+1}{4\pi}\frac{(n-l)!}{(n+l)!}}\mathrm{P}_n^l(\cos\theta_\mathrm{s})\\ &\times\exp(-\mathrm{i}l\varphi_\mathrm{s})\exp(\mathrm{i}m\varphi_\mathrm{s})\,\mathrm{d}\varphi_\mathrm{s}.\end{aligned}\tag{5}$$

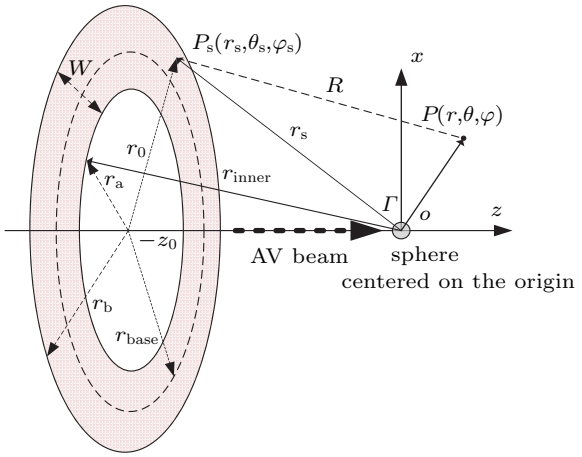


Fig. 1. Schematic diagram of the ARF analysis for AV beams generated by the annular transducer model.

Therefore, according to the orthogonality of $\mathrm{Y}_{nl}(\theta_\mathrm{s},\varphi_\mathrm{s})$, equation (5) can be revised to

$$\begin{aligned}&\int_0^{2\pi}\exp(\mathrm{i}m\varphi_\mathrm{s})\,\mathrm{P}_n(\cos\Gamma)\,\mathrm{d}\varphi_\mathrm{s}\\ =\;&2\pi\frac{(n-m)!}{(n+m)!}\mathrm{P}_n^m(\cos\theta_\mathrm{s})\,\mathrm{P}_n^m(\cos\theta)\exp(\mathrm{i}m\varphi),\end{aligned}\tag{6}$$

where $\mathrm{P}_n^m(x)$ is the associate Legendre function of n-th degree and m-th order. By integrating over the sphere surface, the superimposed velocity potential is achieved by

$$\begin{aligned}&\phi_\mathrm{net}(r,\theta,\varphi)\\ =\;&\mathrm{e}^{-\mathrm{i}\omega t}\,\mathrm{e}^{\mathrm{i}m\varphi}\sum_{n=0}^{\infty}\mathrm{i}\,u_0k_0\frac{(2n+1)}{2}\\ &\times[\,\mathrm{j}_n(k_0r)+s_n\mathrm{h}_n(k_0r)]\,\mathrm{P}_n^m(\cos\theta)\frac{(n-m)!}{(n+m)!}\Lambda_n,\end{aligned}\tag{7}$$

where $\Lambda_n=\int_{r_\mathrm{a}}^{r_\mathrm{b}}\mathrm{h}_n(k_0r_\mathrm{s})\mathrm{P}_n^m(\cos\theta_\mathrm{s})\,r_0\mathrm{d}r_0$ is a constant determined by the geometric configuration of the annular transducer for each term of the series. By varying the result of Λ_n according to the geometry shape of the transducer, the proposed calculation method can be applied to all symmetrical source models which can be described by a rotating body. Therefore, the ARF exerted on the sphere[26,34] can be calculated by

$$\begin{aligned}&\langle F_z\rangle=\langle F_r\rangle+\langle F_\theta\rangle+\langle F_{r,\theta}\rangle+\langle F_t\rangle+\langle F_\varphi\rangle,\\ &\langle F_r\rangle=-\frac{a^2\rho}{2}\left\langle\int_0^{2\pi}\int_0^{\pi}\left(\frac{\partial\phi_\mathrm{net}}{\partial r}\right)^2_{r=a}\sin\theta\cos\theta\,\mathrm{d}\theta\mathrm{d}\varphi\right\rangle,\\ &\langle F_\theta\rangle=\frac{\rho}{2}\left\langle\int_0^{2\pi}\int_0^{\pi}\left(\frac{\partial\phi_\mathrm{net}}{\partial\theta}\right)^2_{r=a}\sin\theta\cos\theta\,\mathrm{d}\theta\mathrm{d}\varphi\right\rangle,\\ &\langle F_{r,\theta}\rangle=a\rho\left\langle\int_0^{2\pi}\int_0^{\pi}\left(\frac{\partial\phi_\mathrm{net}}{\partial r}\right)_{r=a}\left(\frac{\partial\phi_\mathrm{net}}{\partial\theta}\right)_{r=a}\sin^2\theta\,\mathrm{d}\theta\mathrm{d}\varphi\right\rangle,\\ &\langle F_t\rangle=\frac{-a^2\rho}{2c^2}\left\langle\int_0^{2\pi}\int_0^{\pi}\left(\frac{\partial\phi_\mathrm{net}}{\partial t}\right)^2_{r=a}\sin\theta\cos\theta\,\mathrm{d}\theta\mathrm{d}\varphi\right\rangle,\\ &\langle F_\varphi\rangle=\frac{\rho}{2}\left\langle\int_0^{2\pi}\int_0^{\pi}\left(\frac{\partial\phi_\mathrm{net}}{\partial\varphi}\right)^2_{r=a}\cot\theta\,\mathrm{d}\theta\mathrm{d}\varphi\right\rangle,\end{aligned}\tag{8}$$

where $\langle\,\rangle$ is the time-averaged calculation over one period, and the partial derivatives with respect to r, θ, φ, and t can be obtained by

$$\begin{aligned}\frac{\partial\varphi_\mathrm{net}}{\partial r}=&\mathrm{e}^{-\mathrm{i}\omega t}\,\mathrm{e}^{\mathrm{i}m\varphi}\sum_{n=0}^{\infty}\mathrm{i}\,u_0k_0^2\frac{(2n+1)}{2}\left[\,\mathrm{j}_n'(k_0r)+s_n\mathrm{h}_n'(k_0r)\right]\\ &\times\mathrm{P}_n^m(\cos\theta)\frac{(n-m)!}{(n+m)!}\Lambda_n,\\ \frac{\partial\varphi_\mathrm{net}}{\partial\theta}=&\,\mathrm{e}^{-\mathrm{i}\omega t}\,\mathrm{e}^{\mathrm{i}m\varphi}\sum_{n=0}^{\infty}\mathrm{i}\,u_0k_0\frac{(2n+1)}{2}\left[\,\mathrm{j}_n(k_0r)+s_n\mathrm{h}_n(k_0r)\right]\\ &\times\frac{\partial\mathrm{P}_n^m(\cos\theta)}{\partial\theta}\frac{(n-m)!}{(n+m)!}\Lambda_n,\\ \frac{\partial\varphi_\mathrm{net}}{\partial\phi}=&-m\,\mathrm{e}^{-\mathrm{i}\omega t}\,\mathrm{e}^{\mathrm{i}m\varphi}\sum_{n=0}^{\infty}u_0k_0\frac{(2n+1)}{2}\left[\,\mathrm{j}_n(k_0r)+s_n\mathrm{h}_n(k_0r)\right]\\ &\times\mathrm{P}_n^m(\cos\theta)\frac{(n-m)!}{(n+m)!}\Lambda_n,\\ \frac{\partial\varphi_\mathrm{net}}{\partial t}=&\,\omega\,\mathrm{e}^{-\mathrm{i}\omega t}\,\mathrm{e}^{\mathrm{i}m\varphi}\sum_{n=0}^{\infty}u_0k_0\frac{(2n+1)}{2}\left[\,\mathrm{j}_n(k_0r)+s_n\mathrm{h}_n(k_0r)\right]\\ &\times\mathrm{P}_n^m(\cos\theta)\frac{(n-m)!}{(n+m)!}\Lambda_n,\end{aligned}\tag{9}$$

where

$$\frac{\partial\mathrm{P}_n^m(\cos\theta)}{\partial\theta}=\frac{n\cos\theta\mathrm{P}_n^m(\cos\theta)-(n+m)\mathrm{P}_{n-1}^m(\cos\theta)}{\sin\theta}$$

is achieved by the properties of the associated Legendre function.[32,33]

3. Numerical studies

By considering acoustic scattering from the sphere, the acoustic fields of AV beams with different topological charges are simulated. The annular transducer ($f=1$ MHz, $r_\mathrm{a}=5$ mm, $r_\mathrm{b}=15$ mm, $W=10$ mm, $r_\mathrm{base}=10$ mm) is placed at $z_0=-10$ mm in water ($c_0=1479$ m/s, $\rho_0=1000$ kg/m^3). For practical applications in biomedical engineering, drug particles or cells can be treated as elastic spheres in acoustic fields. The parameters of the elastic polyethylene spheres ($k_0a=3$, $c_\mathrm{s}=2000$ m/s, $\rho_\mathrm{s}=980$ kg/m^3) used in numerical studies are close to those of the fluidic ones. For the shear modulus of the elastic spheres is less than 0.2 GPa, the pressure of the transverse waves produced by the spheres is too small to be considered for simplicity. The normalized axial profiles of the velocity potential for AV beams with $m=0$, 1, 2, and 6 scattered by the elastic polyethylene sphere are presented in

Fig. 2. The acoustic interferences of the velocity potential are clearly displayed for all cases. For the AV beam with $m = 0$ as shown in Fig. 2(a), the velocity potential along the z axis is higher for $z < 0$. By introducing the phase term $\exp(\mathrm{i}m\varphi_s)$ with $m = 1$, 2, and 6, obvious velocity potential zeros along the z axis are generated in Figs. 2(b)–2(d). The radius of the vortex center[35,36] increases accordingly with the increase of the topological charge m. Meanwhile, clear velocity potential fluctuations are displayed on the left side of the sphere for $m = 0$ in Fig. 2(a), and the highest value generated by the on-axis acoustic reflection is located at $z = -a$. However, as indicated by the arrows in Figs. 2(b) and 2(c) for the AV beams with a higher topological charge, the on-axis reflection is weakened with strengthened off-axis acoustic scattering around the sphere. Especially, for the case of $m = 6$, the on-axis and off-axis acoustic scattering can hardly be observed around the sphere in Fig. 2(d) due to the much larger radius of the low-level AV center. Thus, the pulling force, which is weakened by the acoustic reflection[15] and strengthened by the off-axis acoustic scattering, is easier to generate by the AV beam with a higher topological charge.

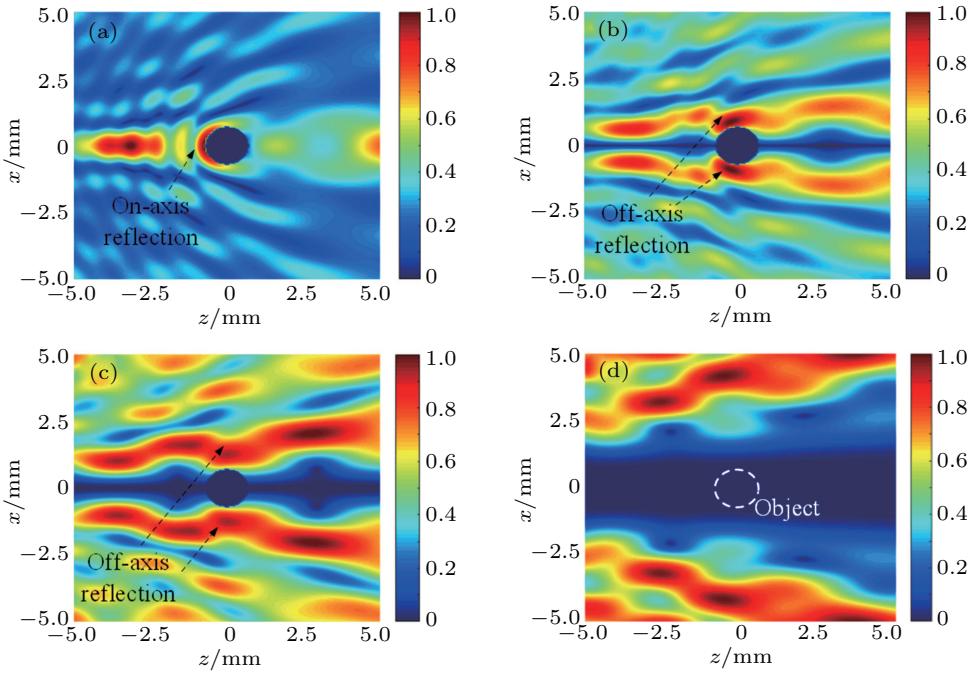


Fig. 2. Axial profiles of the velocity potential for AV beams with the topological charges of (a) 0, (b) 1, (c) 2, and (d) 6 generated by the annular transducer with $W = 10$ mm and $r_{\mathrm{base}} = 10$ mm.

The axial distributions of the ARF with respect to k_0a for AV beams with $m = 0$, 1, 2, and 6 are plotted in Figs. 3(a)–3(d). Affected by the interferences of the acoustic waves radiated from the source elements, obvious ARF fluctuations are displayed for all cases. Since the ARF is the integral of the partial derivatives of φ_{net} over the sphere surface, the ARF increases gradually with the increase of k_0a. Compared with the pushing force, the pulling force is relatively lower as shown in Figs. 3(a)–3(d), which is even too low to be identified for AV beams with $m = 0$, 1, and 2. By extracting the negative value from the ARF, several pulling force areas are displayed as the gray islands in Figs. 3(e)–3(h). It shows that, the pulling force is more likely to exert on the sphere with a smaller k_0a for the AV beam with a higher topological charge. For the AV beam with $m = 0$ as shown in Fig. 3(e), six narrow pulling force islands are displayed in $z_0 < 34$ mm and the ARF appears as the pushing force for $k_0a > 2.3$. By increasing m to 1, several wider pulling force islands are observed in the AV beam with a longer axial distance z_0 as shown in Fig. 3(f). Although the axial distances of the six pulling force islands for $m = 2$ in Fig. 3(g) are similar to those for $m = 1$, the k_0a scopes of the pulling force areas for the AV beam with $m = 2$ are much longer. Especially, due to the low-level velocity potential along the z axis in the AV beam with $m = 6$ as shown in Fig. 2(d), the ARF almost manifests as the pulling force in Fig. 3(h), while the pushing force is formed only for the sphere with a much bigger k_0a at a smaller axial distance.

To analyze the distribution of the pulling force quantitatively, the dimensionless function $Y = 2F_z/\left(\rho_0 k_0^2 q_0^2\right)$[20,21] reflecting both the polarity and the relative amplitude of the ARF is employed and the corresponding axial distributions on spheres with $k_0a = 1$, 2, 3, and 4 for AV beams with $m = 0$, 1, 2, and 6 are plotted in Figs. 4(a)–4(d). The ARF is zero when $z_0 = 0$ for all AV beams due to the geometric symmetry of the annular transducer. With the increase of z_0, obvious ARF fluctuations are displayed with the posi-

tive and negative values representing the pushing and pulling forces. Generally, the number of the pulling force area reduces with the increases of k_0a. For the AV beam with $m = 0$, six pulling force areas with narrow axial regions at (0, 1.6) mm, (4.7, 5.8) mm, (8.6, 9.3) mm, (13.1, 13.7) mm, (19.8, 20.1) mm, and (32.0, 32.2) mm can be observed for $k_0a = 1$, while two pulling force areas at (4.7, 5.3) mm and (8.8, 8.9) mm are presented when k_0a is increased to 2. For $k_0a = 3$ and 4, the ARF always appears as the pushing force, which consists well with the result as illustrated in Fig. 3(a). While, for the AV beam with $m \neq 0$, expanded areas with the negative Y can be produced by the weak on-axis acoustic reflection and the strengthened off-axis acoustic scattering. For a small sphere with $k_0a = 1$, five pulling force areas at (2.4, 4.5), (6.5, 8.4), (10.5, 12.8), (15.8, 19.4) mm and (23.8, 31.5) mm are formed for $m = 1$ as shown in Fig. 4(a), while five and three similar areas for $m = 2$ and 6 with higher force amplitudes at closer axial distances are observed. For the AV beam with a fixed m, the pulling force amplitude decreases with the increase of k_0a with fewer areas. For $k_0a = 2$, five pulling force areas are displayed in Fig. 4(b) for $m = 1$ and 2, while three pulling force areas are formed for $m = 6$. By further increasing k_0a to 3 as shown in Fig. 4(c), the pulling force area disappears for $m = 1$, while five and three areas with reduced force amplitudes at much closer axial distances are formed for $m = 2$ and 6, respectively. In addition, for $k_0a = 4$ as shown in Fig. 4(d), no pulling force areas can be observed for $m \leq 2$. For the AV beam with $m = 6$

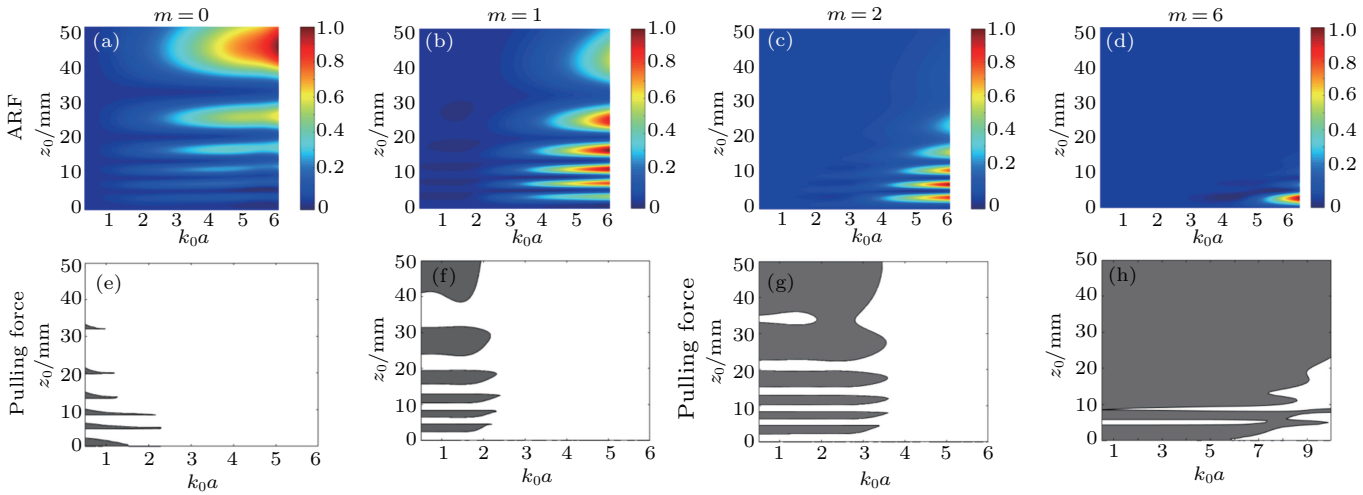


Fig. 3. (a)–(c) Axial distributions of the normalized ARF and (d)–(f) the corresponding pulling force islands with respect to k_0a for AV beams with the topological charges of 0, 1, 2, and 6 generated by the annular transducer with $W = 10$ mm and $r_{\text{base}} = 10$ mm.

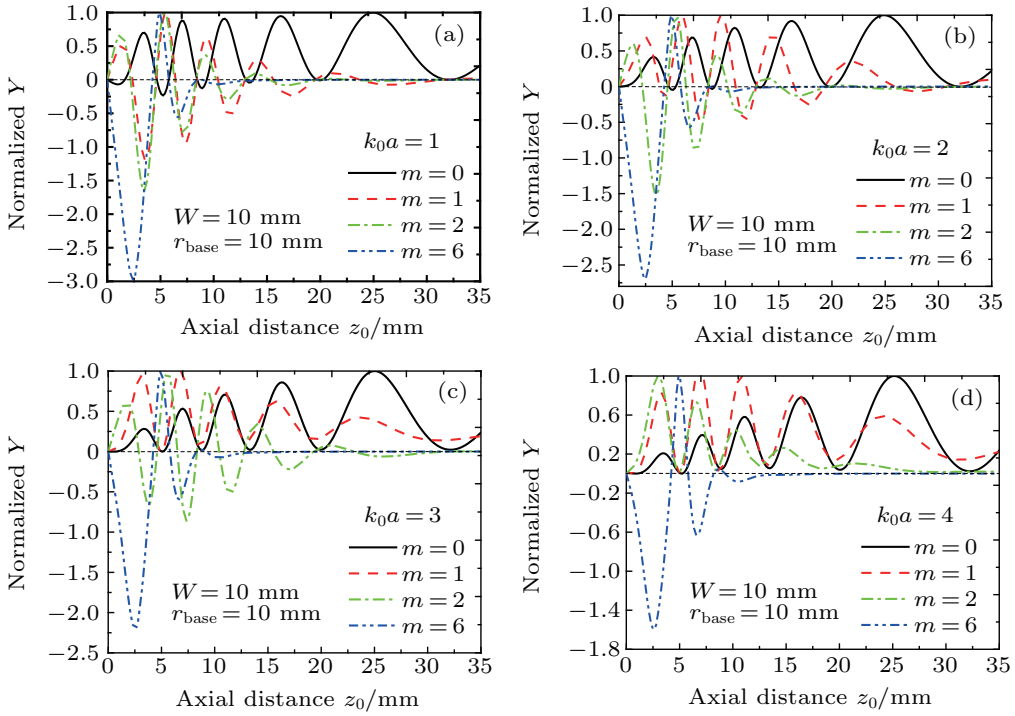


Fig. 4. Axial Y distributions on spheres with $k_0a = 1$ (a), 2 (b), 3 (c), and 4 (d) for AV beams with $m = 0$, 1, 2, and 6 generated by the annular transducer with $W = 10$ mm and $r_{\text{base}} = 10$ mm.

as shown in Figs. 4(a)–4(d), the pulling force can be generated on all spheres from $z_0 = 0$ with the force amplitude decreased with the increases of k_0a and z_0. Especially, for $z_0 > 13.0$ mm, although the ARF mainly appears as the pulling force, it is too low to be applied in practical applications. Thus, it can be concluded that the pulling force is more likely to exert on the sphere with a smaller k_0a for the AV beam with a higher topological charge.

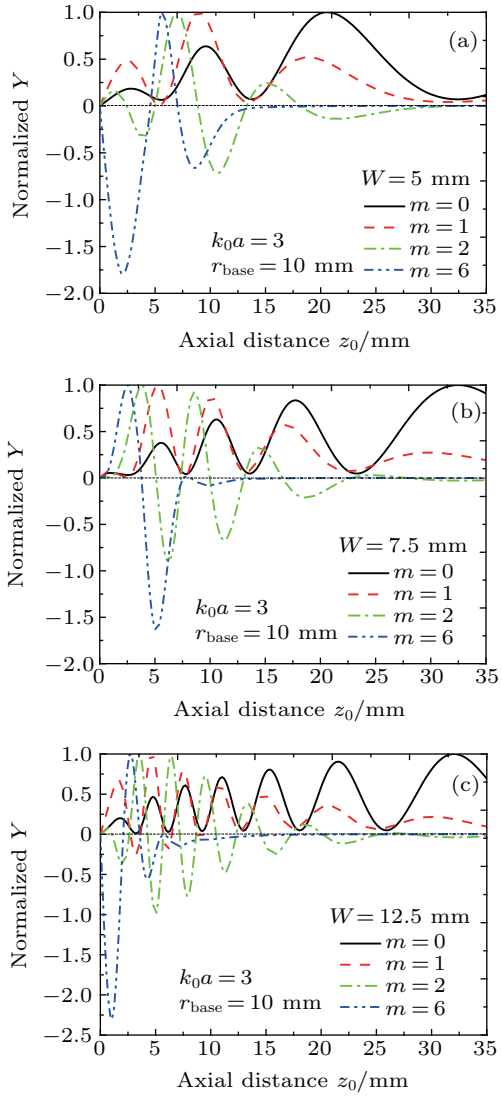


Fig. 5. Axial Y distributions of AV beams with $m = 0$, 1, 2, and 6 generated by the annular transducers with $W = 5$ (a), 7.5 (b), and 12.5 mm (c) for $r_{\text{base}} = 10$ mm.

In addition, in order to analyze the size influence of the annular transducer on the generation of the pulling force, the axial distributions of the ARF on the sphere with $k_0a = 3$ are simulated for the AV beams with $m = 0$, 1, 2, and 6 generated by the annular transducers with various sizes. By fixing $r_{\text{base}} = 10$ mm, the axial Y distributions for the AV beams with various m generated by the transducers with $W =$ 5, 7.5, and 12.5 mm are plotted in Figs. 5(a)–5(c). For $k_0a = 3$ and $W = 5$ mm as plotted in Fig. 5(a), no pulling force area is formed by the AV beams with $m = 0$ and 1, while three pulling force areas with much higher force amplitudes at $(2.5, 4.9)$ mm, $(8.9, 13.1)$ mm, $(18.2, 32.6)$ mm and $(0, 4.6)$ mm, $(7.4, 14.5)$ mm, $(15.1, 35.0)$ mm are produced for $m = 2$ and 6, respectively. With the increase of W, more velocity potential fluctuations are produced by the stronger acoustic interferences of more source elements, resulting in more pulling force areas. When $W = 7.5$ mm, no pulling force area is displayed in Fig. 5(b) for $m = 0$ and 1. Four pulling force areas at $(5.3, 7.4)$ mm, $(10.0, 13.0)$ mm, $(16.6, 22.8)$ mm, and $(27.8, 35.0)$ mm can be observed for $m = 2$, and two pulling force areas at $(3.9, 7.2)$ mm and $(8.9, 13.8)$ mm are observed clearly for $m = 6$. Although Y oscillates around zero, the low-level pulling force disappears gradually with the increase of the axial distance for $z_0 > 13.8$ mm. When $W = 12.5$ mm, two pulling force areas at $(2.8, 3.5)$ mm, $(5.8, 6.5)$ mm for $m = 1$ and seven pulling force areas positioned at $(1.1, 2.5)$ mm, $(4.4, 5.6)$ mm, $(7.4, 8.6)$ mm, $(10.5, 12.3)$ mm, $(14.7, 17.2)$ mm, $(20.1, 25.2)$ mm, and $(28.2, 35.0)$ mm for $m = 2$ are displayed in Fig. 5(c). Similarly, for the case of $m = 6$, three pulling force areas at $(0, 2.8)$ mm, $(3.7, 5.3)$ mm, and $(6.7, 12.4)$ mm are obviously displayed, while the pulling force amplitude is too low to be observed for $z_0 > 12.4$ mm. Thus, for a fixed sphere, more pulling force areas with narrower axial regions and higher force amplitudes can be produced by the annular transducer with a bigger W.

Then, by fixing $W = 10$ mm, the axial Y distributions for AV beams with various topological charges generated by the annular transducers with $r_{\text{base}} = 15$, 20, and 25 mm are illustrated in Figs. 6(a)–6(c). For $r_{\text{base}} = 10$ mm as plotted in Fig. 4(c), five and three pulling force areas can be observed respectively for $m = 2$ and 6. With the increase of r_{base}, the axial regions of the pulling force areas exhibit an expanding tendency. For $r_{\text{base}} = 15$ mm as plotted in Fig. 6(a), four pulling force areas at (5.1, 7.4) mm, $(10.5, 13.1)$ mm, $(16.3, 20.0)$ mm, and $(24.0, 29.8)$ mm for the AV beam with $m = 2$ are observed, and the fifth pulling force area moves out of the observation range ($z_0 > 35$ mm). For $m = 6$, three pulling force areas at $(2.6, 7.2)$ mm, $(9.6, 13.0)$ mm, and $(15.2, 21.2)$ mm are displayed with a rightward tendency of the axial distances. Whereas, for $r_{\text{base}} = 20$ mm, four pulling force areas at $(7.0, 10.0)$ mm, $(14.4, 17.7)$ mm, $(22.0, 26.8)$ mm, $(32.2, 35.0)$ mm, and three pulling force areas at $(4.2, 9.8)$ mm, $(13.1, 17.7)$ mm, $(20.8, 27.5)$ mm with expanded axial regions are clearly shown in Fig. 6(b) for $m = 2$ and 6, respectively. As illustrated in Fig. 6(c) for $r_{\text{base}} = 25$ mm, three pulling force areas at $(9.1, 12.6)$ mm, $(18.0, 22.4)$ mm, $(27.7, 33.6)$ mm, and $(5.4, 12.6)$ mm, $(16.6, 22.4)$ mm, $(26.4, 34.1)$ mm for $m = 2$ and 6 are observed, respectively. Hence, for an elastic sphere, wider pulling force areas can be produced by the annular transducer

with a bigger r_{base}, which can be used to increase the axial distance in object manipulations.

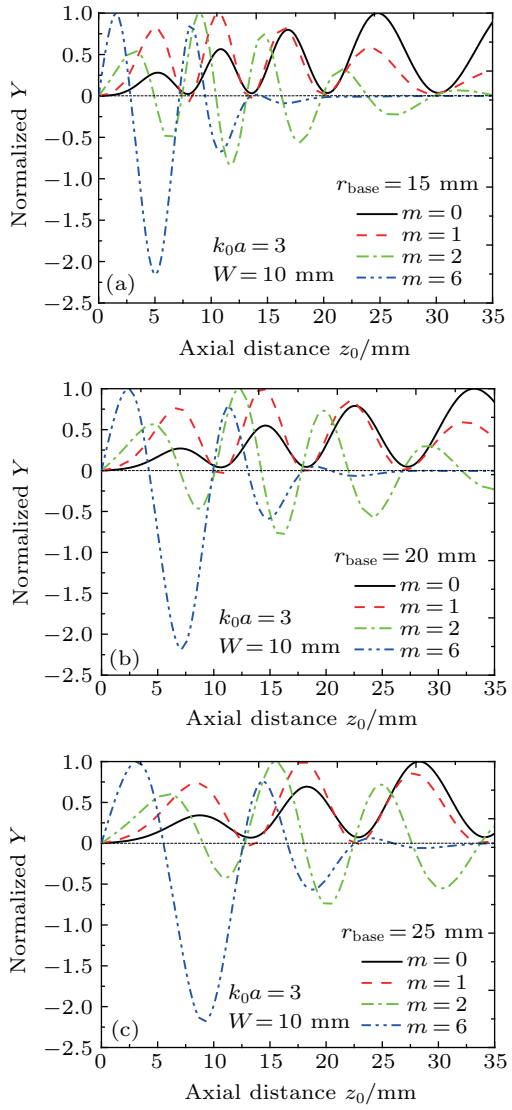


Fig. 6. Axial Y distributions of AV beams with $m = 0$, 1, 2, and 6 generated by the annular transducers with $r_{\text{base}} = 15$ (a), 20 (b), and 25 mm (c) for $W = 10$ mm.

4. Discussion

In this study, the continuous phase variation along the azimuthal direction should be introduced based on the orthogonal properties of the associated Legendre function in the mathematical model. Whereas, it is difficult to generate AV beams of arbitrary orders using the ideal Bessel beam in practical applications. Although the viable approach[1] was developed by physically offsetting the transducer surface, the operating frequency and the topological charge of AV beams cannot be adjusted easily. However, for the phase-coded approach[35–40] using a circular array of sector transducers with a hollow circle at the center,[35] the discrete phase variation produced by the limited number of sources can be used to generate the AV beam with a controllable topological charge. For an N-element source array, the phase difference between adjacent sector transducers is $2\pi m/N$ and the initial phase of each sector source is a fixed value. The acoustic velocity potential and the axial ARF of the AV beam can be achieved based on the acoustic radiations from all the sector sources using the integral calculation. It is reported that circular phase linearity[40] around the center axis of the AV beam can be improved by increasing the source number of the transducer array. When the number of the sector sources is larger enough ($N \geq 8$),[35] the discrete phase variation can be equivalent to a quasi-continuous one to satisfy the requirements of the proposed annular transducer model for AV generation.

Moreover, theoretical simulations of the ARF exerted on centered elastic spheres prove that the pulling force can be generated in AV beams of arbitrary orders with the amplitude and the axial regions determined by the physical parameters of the annular transducer and the elastic sphere and the topological charge of the system. Due to the weakened on-axis acoustic reflection and the strengthened off-axis acoustic scattering, the pulling force is easier to exert on the sphere with a smaller k_0a for the AV beam of a higher order. More pulling force areas with wider axial regions and higher force amplitudes can be produced by the bigger-sized transducer with a bigger r_{base} and a wider W. Then, by fixing r_{b} and decreasing r_{a} to 0 as a special case, more pulling force areas at closer axial distances with higher pulling force amplitudes can be generated by the circular piston transducer with a bigger width W. The generation of near-field multiple traps of paraxial AVs[35] with strengthened gradient force was proved by Wang *et al.* using an 8-elemnet circular sector transducer array, which provided experimental basis for further applications of the proposed annular model. Also, by adjusting the physical parameters of the transducer and the k_0a value of the elastic spheres, the number and the locations of pulling force areas can be controlled accurately on the axis of the AV beam. The balance positions of ARF zero between the pushing and pulling forces can be regarded as the trapping wells for stable object manipulations in three dimensions. Thus, the particles with a similar k_0a can be trapped at multiple positions along the beam axis by the radial and axial radiation force, and the real-time adjustment of particle trapping can also be realized by changing the topological charge of the AV beam.

5. Conclusion

In order to solve the difficulty of generating an ideal Bessel AV beam, an annular transducer model is proposed to study the pulling force along the center axis for the AV beam of an arbitrary order. The ARF exerted on an elastic sphere centered on the AV beam is studied based on acoustic scattering. The axial distributions of the ARF and the corresponding pulling force exerted on spheres with various k_0a are simulated for AV beams with different topological charges. It is proved

that the pulling force can be generated in the AV beam of an arbitrary order with multiple axial regions, and it is more likely to exert on the sphere with a smaller k_0a for the AV beam of a higher order. For an AV beam, the pulling force decreases with the increase of the axial distance for the sphere with a bigger k_0a. More pulling force areas with wider axial regions can be formed by a bigger-sized annular transducer. Although only the cases of specific orders are investigated in this study, the formation principle of the pulling force can be extended to AV beams of arbitrary orders. The theoretical results demonstrate the feasibility of generating the pulling force along the axis of the AV beam, and suggest application potentials of multi-position stable object manipulations using the experimentally applicable circular array of planar transducers.

References

[1] Hefner B T and Marston P L 1999 *J. Acoust. Soc. Am.* **106** 3313
[2] Zhang L and Marston P L 2011 *Phys. Rev. E* **84** 065601
[3] Marchiano R and Thomas J L 2005 *Phys. Rev. E* **71** 066616
[4] Lekner J 2006 *J. Acoust. Soc. Am.* **120** 3475
[5] Marchiano R, Coulouvrat F, Ganjehi L and Thomas J L 2008 *Phys. Rev. E* **77** 016605
[6] Demore C E M, Yang Z, Volovick A, Cochran S, MacDonald M P and Spalding G C 2012 *Phys. Rev. Lett.* **108** 194301
[7] Volke-Sepúlveda K, Santillán A O and Boullosa R R 2008 *Phys. Rev. Lett.* **100** 024302
[8] Santillán A O and Volke-Sepúlveda K 2009 *Am. J. Phys.* **77** 209
[9] Li W, Dai S, Ma Q, Guo G and Ding H 2018 *Chin. Phys. B* **27** 024301
[10] Kang S T and Yeh C K 2010 *IEEE Trans. Ultrason. Ferr. Freq. Contr.* **57** 1451
[11] Baresch D, Thomas J L and Marchiano R 2013 *J. Appl. Phys.* **113** 184901
[12] Skeldon K D, Wilson C, Edgar M and Padgett M J 2008 *New J. Phys.* **10** 013018
[13] Courtney C R P, Demore C E M, Wu H, Grinenko A, Wilcox P D, Cochran S and Drinkwater B W 2014 *Appl. Phys. Lett.* **104** 154103
[14] Lee J, Ha K and Shung K K 2005 *J. Acoust. Soc. Am.* **117** 3273
[15] Sapozhnikov O A and Bailey M R 2013 *J. Acoust. Soc. Am.* **133** 661
[16] Mitri F G 2008 *Ann. Phys.* **323** 1604
[17] Mitri F G 2015 *IEEE Trans. Ultrason. Ferr. Freq. Contr.* **62** 1827
[18] Silva G T and Baggio A L 2015 *Ultrasonics* **56** 449
[19] Nye J F and Berry M V 1974 *Proc. R. Soc. Lond. A* **336** 165
[20] Marston P L 2006 *J. Acoust. Soc. Am.* **120** 3518
[21] Marston P L 2007 *J. Acoust. Soc. Am.* **122** 3162
[22] Marston P L 2009 *J. Acoust. Soc. Am.* **125** 3539
[23] Zhang L and Marston P L 2011 *Phys. Rev. E* **84** 035601
[24] Zhang L and Marston P L 2012 *J. Acoust. Soc. Am.* **131** EL329
[25] Mitri F G 2009 *J. Phys. A: Math. Theor.* **42** 245202
[26] Mitri F G 2009 *Ultrasonics* **49** 794
[27] Mitri F G 2009 *IEEE Trans. Ultrason. Ferr. Freq. Contr.* **56** 1059
[28] Baresch D, Thomas J L and Marchiano R 2016 *Phys. Rev. Lett.* **116** 024301
[29] McGloin D and Dholakia K 2005 *Contemp. Phys.* **46** 15
[30] Cheng J 2011 *Principles of acoustics* (Beijing: Science Press) pp. 247–270
[31] Zang Y, Qiao Y, Liu J and Liu X 2019 *Chin. Phys. B* **28** 034301
[32] Jackson J D 1999 *Classical electrodynamics*, 3rd edn. (New York: Wiley) pp. 96–101
[33] Arfken G B, Weber H J and Harris F E 2013 *Mathematical methods for physicists* (Boston: Academic Press) pp. 715–736
[34] Wang H, Liu X, Gao S, Cui J, Liu J, He A and Zhang G 2018 *Chin. Phys. B* **27** 034302
[35] Wang Q, Li Y, Ma Q, Guo G, Tu J and Zhang D 2018 *J. Appl. Phys.* **123** 034901
[36] Yang L, Ma Q, Tu J and Zhang D 2013 *J. Appl. Phys.* **113** 154904
[37] Zheng H, Gao L, Ma Q, Dai Y and Zhang D 2014 *J. Appl. Phys.* **115** 084909
[38] Li Y, Guo G, Ma Q, Tu J and Zhang D 2017 *J. Appl. Phys.* **121** 164901
[39] Li Y, Guo G, Tu J, Ma Q, Guo X, Zhang D and Sapozhnikov O A 2018 *Appl. Phys. Lett.* **112** 254101
[40] Gao L, Zheng H, Ma Q, Tu J and Zhang D 2014 *J. Appl. Phys.* **116** 024905